Rain Evaporation Rate Estimates from Dual-Wavelength Lidar Measurements and Intercomparison against a Model Analytical Solution

S. LOLLI[a]

Joint Center for Earth Systems Technology, University of Maryland, Baltimore County, Baltimore, Maryland

P. DI GIROLAMO

Scuola di Ingegneria, Università degli studi della Basilicata, Potenza, Italy

B. DEMOZ

Joint Center for Earth Systems Technology, University of Maryland, Baltimore County, Baltimore, Maryland

X. LI

GESTAR, NASA GSFC, Greenbelt, Maryland

E. J. WELTON

Code 612, NASA GSFC, Greenbelt, Maryland

ABSTRACT

Rain evaporation, while significantly contributing to moisture and heat cloud budgets, is a still poorly understood process with few measurements presently available. Multiwavelength lidars, widely employed in aerosols and clouds studies, can also provide useful information on the microphysical characteristics of light precipitation, for example, drizzle and virga. In this paper, lidar measurements of the median volume raindrop diameter and rain evaporation rate profiles are compared with a model analytical solution. The intercomparison reveals good agreement between the model and observations, with a correlation between the profiles up to 65% and a root-mean-square error up to 22% with a 5% bias. Larger discrepancies are due to radiosonde soundings different air masses and model assumptions no more valid along the profile as non-steady atmosphere and/or appearance of collision–coalescence processes. Nevertheless, this study shares valuable information to better characterize the rain evaporation processes.

1. Introduction

The water cycle describes the fluxes and movement of water in its three different aggregation phases (liquid, solid, and gaseous) inside Earth's atmosphere. It refers to the continuous water mass exchanges between the atmosphere, the oceans, Earth's surface, and the underground waters. Besides water accumulation in the oceans, terrestrial water is also involved in multiple cycles, moving water between different reservoirs through the physical processes of condensation, precipitation, evaporation, and runoff. An adequate understanding and improved prediction capability of these processes are fundamental to maintaining sustainable water resources on Earth. The contribution of rain evaporation to the heat and moisture budgets of clouds, to the atmospheric moisture cycling and latent heating, is fundamental but very few measurements of these processes are presently available (Xie et al. 2016; Worden et al. 2007). Cloud lifetime is very sensitive to

Denotes content that is immediately available upon publication as open access.

drizzle and virga precipitation rates, as these forms of rain remove water from the cloud base, and cold pools and currents formed from subcloud evaporation may also contribute to convection regenerations (Li et al. 2009; Morrison et al. 2009). Moreover, virga represents an aviation hazard, as in certain conditions of this type of precipitation can generate strong local microbursts (Bedard 2003). The few available measurements of the abovementioned processes have been carried out using either in situ sensors or radars. For what concerns in situ measurements, Blanchard (1953), Gori and Joss (1980), and Levin et al. (1991) estimated rain evaporation rates by measuring drop size distributions (DSDs) along a mountain slope. However, these in situ measurements are limited in space and time. Remote estimates of rain evaporation rates can be determined from rainwater content profiles obtained from radar reflectivity measurements (Leary and Houze 1979) and DSD profilers, as well as dual-polarization radar measurements (Xie. et al. 2016). However, this approach may lead to large errors in the estimate rain evaporation rates if a fixed relationship between radar reflectivity and rainwater content is assumed along the vertical path (Li and Srivastava 2001). In this direction, Li and Srivastava (2001) determined an approximate analytical solution for the estimation of the evaporation rate of a single raindrop based on the consideration of the thermodynamic equations, which control atmospheric conditions. Beyond these attempts, no further achievements have been done in terms of evaporation retrievals, despite its huge importance for a correct assessment of the atmospheric water and energy cycles.

In this paper we describe an application of the color ratio (CR) technique (Lolli et al. 2013a) for the estimation of rain evaporation rates based on the use of a dual-wavelength lidar, which is an active optical device particularly suited to investigate atmospheric constituents, especially aerosols (Di Girolamo et al. 1995; Lolli et al. 2013b, 2014a,b; Tan et al. 2014) and clouds (Lolli et al. 2016). Several authors (Demoz et al. 2000; Di Girolamo et al. 2012a; Lolli et al. 2013a) reported lidar measurements during light precipitation events, for example, drizzle and virga. In particular, Lolli et al. (2013a) developed a technique to retrieve the median volume raindrop diameter profile from the measurements performed by two collocated commercial lidars operating at 355 and 532 nm, respectively. This technique allows for retrieving the median volume raindrop diameter profile and, consequently, the evaporation rate, which in turn is used to validate the model analytical solution.

The main objective of this paper is to compare quantitatively estimates of the median volume drop diameter profile obtained from lidar measurements with those determined with the analytical model proposed by Li and Srivastava (2001), and to discuss possible discrepancies between the two. Once assessed how the analytical model performs with respect to a multiwavelength lidar, it will be possible to extend this concept to the estimation of the rain evaporation rate from singlewavelength lidars, in combination with ground-based sensors and the above-mentioned analytical model. For this method, to be effective, the precipitation should reach the ground (to be measured by the disdrometer) with low intensity (as higher intensity will extinguish the lidar signal). From the disdrometer DSD measurements, it is possible to reconstruct the median volume raindrop diameter profile at different altitudes through the model analytical solution and then the evaporation rate up to the cloud base just knowing the thermodynamics of the atmosphere. The lidar measurements are of fundamental importance because they will be used to determine the cloud-base height with much higher accuracy with respect to other techniques, for example, the radiosonde. As the analytical model raindrop diameters are very sensitive to the atmospheric layer thickness, a few hundred meters of error in determining the cloud-base height could introduce significant errors into the evaporation rate calculation.

Thus, this work represents the first step in developing a method to retrieve light rain evaporation rates that combines observations from single-wavelength backscatter lidars (Lolli et al. 2013a), as those deployed in the frame of the NASA Micropulse Lidar Network (MPLNET; Welton et al. 2002; Campbell et al. 2002), and those the analytical evaporation model developed by Li and Srivastava (2001). The successful application of this technique may lead to the inclusion of this information among the additional products provided by the MPLNET and/or other lidar networks. If properly implemented in these networks, a comprehensive dataset on raindrop size and rain evaporation rates could be collected and used to test and ultimately improve the parameterization schemes of evaporation processes in numerical weather prediction (NWP) and climate models.

2. Method

Several approaches to retrieve the median volume raindrop diameter D_0 during light precipitation events using lidar backscatter data using two different wavelengths have been illustrated by several authors (Lolli et al. 2013a; Westbrook et al. 2010; O'Connor et al. 2005). All these approaches take advantage of the variability of the differential backscattering efficiency at the two wavelengths over the DSD [UV_{355nm}–VIS_{532nm} in Lolli et al. (2013a); IR_{905nm}–IR_{1500nm} in Westbrook et al. (2010)]. For example, the approach reported by Lolli et al. 2013a relies on the consideration that the
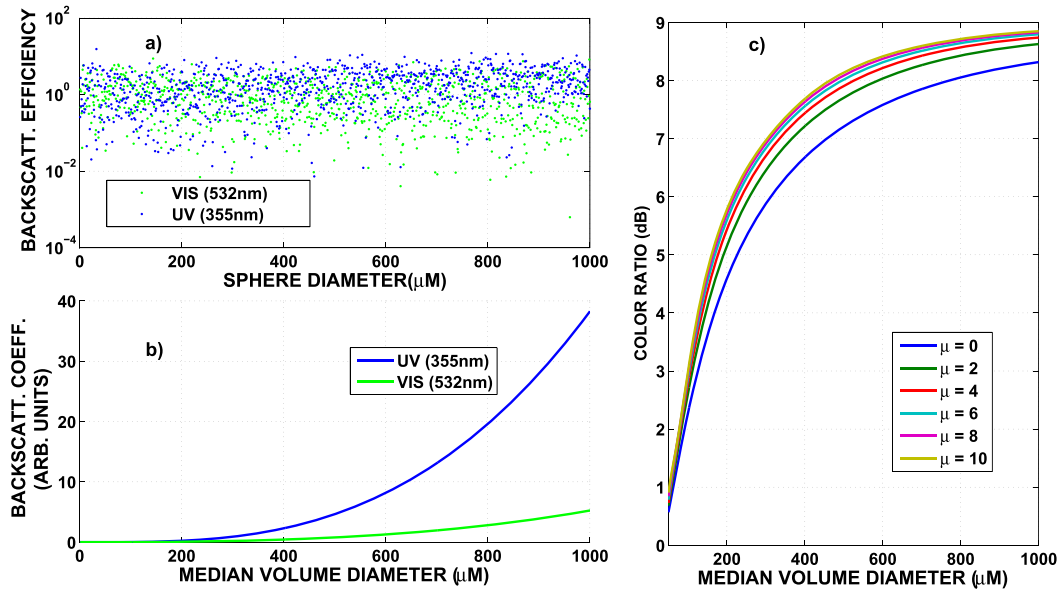
FIG. 1. (a) Backscattering efficiencies obtained with Mie code vs sphere diameter for 532 (green dots) and 355 nm (blue dots). (b) Backscattering coefficient vs the median volume at 355 and 532 nm. (c) The CR obtained from the ratio of the two rain backscattering coefficients in (b) for different values of the shape parameter μ of the gamma raindrop distribution.

backscattering efficiency at 532 nm is on average much less sensitive to the water sphere diameter with respect to the same variable at 355 nm (while the extinction coefficient is wavelength independent). This is depicted in Figs. 1a and 1b, where it is visible how the backscattering efficiencies calculated using an algorithm based on Mie theory for large particles with respect to the sounding wavelength (Lolli et al. 2013a) are dependent on the water sphere diameter at 355 (blue dots) and 532 nm (green dots). The theoretical rain backscattering coefficient (last term of the right side of Eq. (2); raindrops are supposed to be spherical) is obtained by integrating the values of the backscattering efficiencies (Fig. 1a) over the minimum and maximum values of the raindrop size distribution (here assumed to be a gamma function, with raindrop diameters ranging from 1 to 1000 μm). The result of the integration is showed in Fig. 1b, for the two wavelengths of interest, in function of D_0, a parameter of the gamma raindrop distribution [see Eq. (4) below]. As the differences between the backscattering coefficients in function of D_0 become substantial, it is possible to define the color ratio [Fig. 1c; Eq. (5)] as 10 times the logarithm of the ratio of the rain backscattering coefficients at the two wavelengths. By inverting the measured color ratio, it will be possible to retrieve the median volume raindrop diameter at each range bin using the curves in Fig. 1c as lookup tables. Accurate information on the method is beyond the scope of this

paper and can be found in Lolli et al. (2013a). Subsequently, the evaporation rate can be estimated as the change of the raindrop volume (shrinking/growing) during precipitation along the profile for each of the two adjacent levels as

$$E(r) = \frac{(d_{r+1})^3 - d_r^3}{(d_{r+1})^3},$$ (1)

where the subscripts r and $r + 1$ indicate the raindrop diameter d at current range bin r and immediately above $(r + 1)$. The evaporation is closely related to the humidity content of the surrounding atmosphere and the atmospheric processes of breakdown or coalescence. The raindrop diameter and evaporation retrieved by lidar with the method described above can be finally compared with the analytical solution model proposed by Li and Srivastava (2001).

a. Lidar measurements

The intercomparison was performed for two selected case studies. The first one refers to the lidar measurements carried out during the Convective and Orographically Induced Precipitation Study (COPS), which took place in southern Germany and eastern France from May to August 2007 (Kalthoff et al. 2011; Wulfmeyer et al. 2011; Di Girolamo et al. 2012a). The multiwavelength University of Basilicata (BASIL) Raman lidar (Di Girolamo et al. 2009a,b), taking advantage of

the rotational and vibrational Raman techniques, provides high-resolution and accurate profile measurements of the particle backscattering coefficient at 355, 532, and 1064 nm (Di Girolamo et al. 2012b), which are determined based on the application of a Klett-modified approach to the collected elastic signals at these wavelengths (Di Girolamo et al. 1995). The IR (1064 nm) channel measurements cannot be exploited, as these measurements may be slightly affected by multiple scattering effects associated with the use of a wider field of view. The measurement uncertainty affecting the particle backscattering coefficient is in the range of 3%–5% along the vertical region of interest, from the surface up to the cloud base.

For the second selected case study, the lidar measurements were collected at the NASA Goddard Space Flight Center MPLNET permanent observational site, where a 355-nm commercial single-wavelength elastic backscattering lidar (Lolli et al. 2011) was collocated with a single-wavelength 532-nm commercial Micropulse Lidar (Spinhirne 1993; Spinhirne et al. 1995). In both cases, the color ratio, obtained from the ratio of the rain backscattering coefficient profiles [Eq. (2)] at 355 and 532 nm—$\beta_{355}(r)$ and $\beta_{532}(r)$, respectively—is used to determine the median volume raindrop diameter profile. During the precipitation, at a certain range r below the cloud base, the total backscattering coefficient β_{tot} is defined as the sum of three major contributions (the contributions from other gases present in the atmosphere are assumed negligible),

$$\beta_{tot}(r) = \beta_{mol}(r) + \beta_{aer}(r) + \beta_{rain}(r). \qquad (2)$$

The aerosol contribution β_{aer} is assumed to be constant during the precipitation event (no scavenging effects, which is a reasonable assumption, as raindrops are submillimetric), and it is determined during a short time interval (usually 5 min) before and after (when possible) the precipitation event. The retrieval is not unique but dependent on the considered lidar technique (Raman or elastic). The molecular contribution β_{mol} has an analytical solution depending on the density of the atmosphere, and it can be easily determined from ancillary data—for example, from those provided by a simultaneous and collocated radiosonde; it is then possible to isolate β_{rain}, that is, the rain contribution to the total backscattering coefficient. A more detailed description and a discussion on retrieval errors can be found in Lolli et al. (2013a). However, the Raman lidar system BASIL is not equipped to operate during rain episodes (no rain window is present) and can run only until the precipitation reaches the ground or during virga episodes.

Both case studies presented in this paper represent virga rain episodes (see more details below).

b. Analytical model

The analytical model determines the "evaporation power" of a stationary atmospheric layer, based on the computation of the single raindrop diameter D^* (dependent only on temperature and water vapor), defined as the diameter of a single raindrop fully evaporating in the selected layer (Li and Srivastava 2001). The model relies on the assumption of a steady environment with negligible vertical air motion. In the study by Li and Srivastava (2001), these conditions were assumed to be valid for stratiform rain, but in the present paper these conditions are also applied to selected virga episodes. Instead of calculating D^*, in this study we compute the temporal evolution of each single-raindrop diameter present in the precipitation at each different atmospheric layer, from cloud base to complete evaporation using a more general equation [Eq. (3)]. The thickness of each layer is defined from the radiosonde spatial resolution. The temporal evolution of the raindrop diameter depends only on the thermodynamics properties of the considered atmospheric layer (measured by the radiosonde). A raindrop diameter D_1 at cloud base (at a certain altitude h_1) evolves into diameter D_2, at the bottom of the first considered layer (at a certain altitude h_2). Then D_2 becomes the input diameter of the top of the second considered layer and so on, down to the last available layer before complete evaporation. The thermodynamic properties of the atmospheric layer with a thickness defined by $h_1 - h_2$ are determined from the radiosonde.

As the method is suitable only for light precipitation events (Lolli et al. 2013a), we assume that at cloud base the distribution of raindrop diameters ranges from 1 to 1000 μm. We end up calculating the whole atmospheric profile of each D from cloud base to complete evaporation (or more general to the ground) through

$$(c_2 D_1^2 + c_1 D_1) - (c_2 D_2^2 + c_1 D_2) = E(h_1, h_2), \qquad (3)$$

where h_1 is the upper limit of the considered layer and h_2 is its lower limit. The coefficients c_1 and c_2 are completely determined from the atmospheric temperature and pressure values at the center of the layer, while E is a quantity depending only on the vertical variability of water vapor, temperature, and pressure between the levels h_1 and h_2 (Li and Srivastava 2001). Runs for different assigned thermodynamic variables of the analytical model put in evidence a higher sensitivity of the model to the relative humidity (8% for 10% change),
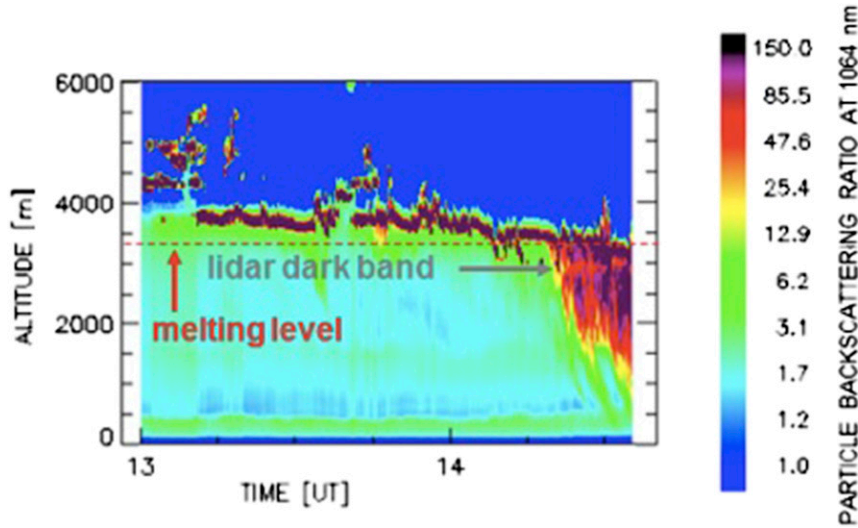
FIG. 2. Time evolution of the particle backscattering ratio at 1064 nm for the time interval 1300–1435 UTC 23 Jul 2007 as measured by the lidar system BASIL.

then pressure (4% for 10% change) and temperature (3% for 10% change).

We suppose that during the precipitation event, the raindrops follow a modified normalized gamma DSD (Lolli et al. 2013a; Bringi and Chandrasekar 2001; Ulbrich and Atlas 1998; Marshall and Palmer 1948),

$$\frac{\Delta N}{\Delta D}(N_0, D, D_0, \mu) = N_0 \left(\frac{D}{D_0}\right)^{\mu} \exp\left[-\frac{(3.67 + \mu)}{D_0}D\right],$$
(4)

where D_0 is the median raindrop volume diameter and μ is the size dispersion parameter ($\mu = 0$ corresponds to a Marshall–Palmer distribution; Marshall and Palmer 1948), while $\Delta N \Delta D$ represents the number of drops with a diameter between D and $D + \Delta D$ and N_0 is the total drop concentration for a given (D_0, μ). If a raindrop diameter becomes negative after traveling a certain distance below the cloud base, it means that that raindrop is completely evaporated and then the considered diameter will no more be taken into account in the calculation. To compare the model analytic solution with the lidar-retrieved raindrop diameter, the median volume raindrop diameter is calculated at each range bin. This is computed as that value separating the total water volume with respect to the droplet spectrum in two identical parts (or the raindrop diameter value for which the cumulative frequency is equal to 0.5).

3. Intercomparisons

On 23 July 2007 (first case study; Di Girolamo et al. 2012a), a cyclonic system, developed in the northern Atlantic region, moved toward the COPS measurement site, producing stratiform clouds with consequent stratiform rain occurring in the afternoon. These steady meteorological conditions are optimal for applying the analytical model. Figure 2 illustrates the time evolution of the particle backscattering ratio at 1064 nm for the time interval 1300–1435 UTC. The particle backscattering ratio, defined as the ratio of the particle backscattering coefficient over the molecular backscattering coefficient, quantifies the quantity of the particle optical loading in the atmosphere (Di Girolamo et al. 1995). The figure clearly reveals the presence of a lidar dark band (Di Girolamo et al. 2012a) around 2.8 km, associated with changes in scattering properties of precipitating hydrometeors taking place in the melting layer during the snowflake-to-raindrop transition. This figure also reveals the presence of stratiform clouds, with a cloud base at 3.1–3.3 km above ground level (AGL). Ancillary information on the thermodynamic state of the atmosphere was provided by ad hoc radiosondes, launched every 3 h during the measurement session (Di Girolamo et al. 2012a). The median volume raindrop diameter profile is determined at each range bin from the lidar color ratio CR, this latter quantity being defined as 10 times the logarithm of the power ratio of the rain backscattering coefficients at the two considered wavelengths [Eq. (5)]. The analytical expression relating CR to D_0 is the following:

$$CR(D_0) = 10 \log_{10}\left(\frac{\beta_{355\text{rain}}}{\beta_{532\text{rain}}}\right),$$
(5)

where $\beta_{355\text{rain}}$ and $\beta_{532\text{rain}}$ are the rain contribution to the total backscattering coefficients at 355 and 532 nm,
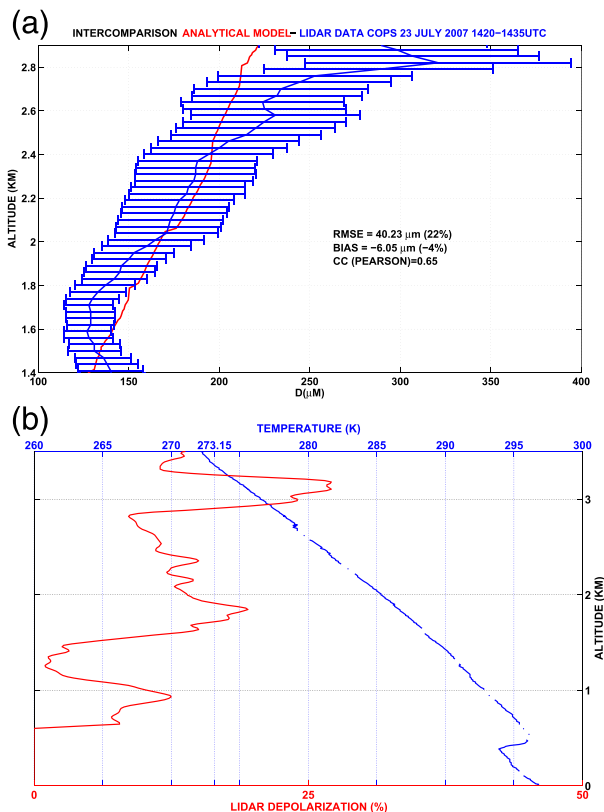
FIG. 3. (a) Vertical profile of the median volume raindrop diameter D_0 (blue line, with error bar) as determined from the lidar measurements on 23 Jul 2007 and the model analytical solution (red line). The green dashed line marks the transition altitude approximately at 2.65 km where rimed aggregate snowflakes start to melt into raindrops. (b) Vertical profiles of atmospheric temperature (from the radiosonde launched at 1406 UTC; blue) and lidar depolarization (red).

respectively [defined in Eq. (3); see also Lolli et al. 2013a]. To each lidar retrieved CR (that represents a point in Fig. 1c), will correspond Six different D_0 values (see the six different curves in Fig. 1c) because the size dispersion parameter μ is a priori unknown. Term D_0 is calculated as the average between those six different values, and the uncertainty is the half difference between the largest and the smallest raindrop diameter values. Again, a more detailed explanation can be found in Lolli et al. (2013a).

On 23 July 2007, CR was determined over a time interval of 15 min, from 1420 to 1435 UTC. The lidar integration time (15 min) was selected in order to be comparable with the time experienced by the radiosonde to cover the vertical interval of interest for this study. The radiosonde was launched at 1406 UTC and was considering an ascent speed of $4\,\mathrm{m\,s^{-1}}$ (that translates into a spatial resolution of about 15 m); 15 min is in fact the time needed by the radiosonde to cover the

vertical interval from the surface up to 3.6 km—this being the vertical region of interest considered in our study. Figure 3b also illustrates the vertical profile of temperature as measured by the radiosonde that provides quantitative information on the thermodynamic conditions in the altitude region under investigation (the melting level, i.e., the 0°C isotherm level is located at 3.35 km AGL). The profile of the raindrop diameter corresponding to the above-estimated CR profile is illustrated in Fig. 3a (blue line) with the error bars accounting for the overall error affecting the color ratio measurement. This error includes the signal measurement uncertainty, the two-way transmission error, and the atmospheric density uncertainty. The random uncertainty affecting lidar signal measurements can be quantified at each altitude level through Poisson statistics; the uncertainty affecting molecular backscattering is related to the molecular density uncertainty. The aerosol transmission error is assumed to be constant (8%; Lolli et al. 2013a,b), while the molecular transmission error is again related to the one affecting molecular density. The median volume raindrop diameter ranges from 100 to 350 μm. It is to be pointed out that the 15-min integration time interval considered for the determination of the median volume raindrop diameter (1420–1435 UTC) includes lidar profiles during both the virga event and afterward. In fact, since the Raman lidar was not equipped to operate during precipitation episodes, measurements were stopped as soon as the first raindrops reached the ground. These drops do not evaporate before reaching the ground and, consequently, strictly speaking, they do not fall into the category of virga. These drops take approximately 8 min to cover the vertical region from 2.9 km to the ground. Consequently, only the first 7 min out of the 15-min total integration time exclusively include lidar profiles from the virga episode, while the following 8 min include profiles characterized by the coexistence of virga and nonvirga particles. However, this particle coexistence has no implication on the results illustrated here. To better understand this point, it is to be pointed out that the evaporation or sublimation of the melting particles during the virga event is accompanied by the absorption of latent heat, which ultimately leads to a progressive cooling of the lower atmospheric layers. This is especially true below 1.5 km, as most hydrometeors are found to evaporate/sublimate below this altitude. Thus, precipitating hydrometeors are found to fall in a progressively cooler environment, which is no longer able to permit particles' evaporation or sublimation, and they finally reach the ground. In any case, environmental cooling has marginal effects on the raindrop diameter results, illustrated in Fig. 3, which includes only results
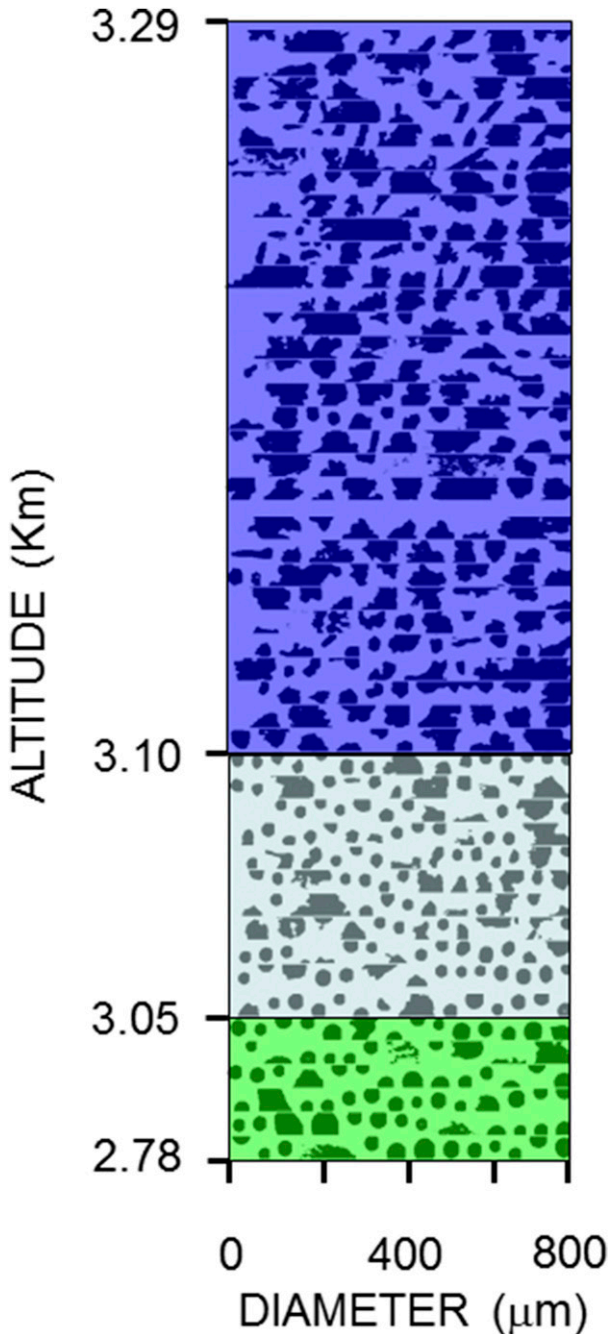
FIG. 4. Two-dimensional footprints of the melting hydrometeors during the snowflake-to-raindrop transition. The shadowed areas identify different sounded vertical intervals characterized by different precipitating particle types and properties (more information in Di Girolamo et al. 2012b). Blue shadowed area: rimed aggregate snowflakes; light blue shadowed area: mixed rain drops with few rimed aggregates; green shadowed area: rain drops.

in the altitude region 1.4–2.9 km, which is a region where thermal effects on the melting environment associated with the hydrometeors' absorption of latent heat are limited.

The reduction of the raindrop diameter discussed above is also well represented in Fig. 4, illustrating the two-dimensional hydrometeors' footprints collected by the in situ two-dimensional cloud (2DC) probe on board the scientific research aircraft ATR42 from Service des Avions Français Instrumentés pour la Recherche en Environnement (SAFIRE). The 2DC probe includes a linear array of 30 photodiodes (each of 25-μm diameter, with a total length of 800 μm) located in front of a second array of diode lasers illuminating the photodiodes. When precipitating particles pass in between the two arrays, a certain number of photodiodes are shadowed and footprints of the particles are generated. Based on this methodology, 2DC probes provide two-dimensional images of the atmospheric precipitating particles, with a maximum detectable particle size of 2 mm. These measurements can be used to retrieve the precipitating particle size distribution. The 2DC probe data in Fig. 4 clearly highlight the progressive melting of snowflakes into raindrops of smaller size.

It is important to stress that melting occurs primarily near the cloud base, up to an altitude of 2.75 km. This is the cutoff altitude at which the melting process ends, with just liquid drops being present below. This is indicated by the lidar depolarization profile (also illustrated in Fig. 3b), with values in the range 25%–30% high in the melting layer, where particles are not completely melted, and values of 5%–10% below 2.8 km (these low values indicate spherical liquid raindrops).

These values are in good agreement with those reported for the same case study by Di Girolamo et al. (2012a), based on the data collected by the in situ 2DC probe. The aircraft measurements were carried out approximately half an hour after the lidar measurements (as in fact the lidar was not operational after 1435 UTC because the rain was reaching the ground) and the footprint on ground of the aircraft was located at a distance of approximately 10–15 km from the lidar station. More specifically, Di Girolamo et al. (2012a) reported values of D_0 of 305 and 278 μm at 3.05 and 2.78 km, respectively, as obtained by fitting a Marshall–Palmer function to the time series of the two-dimensional images represented as a DSD. However, we believe that in the presence of stratiform precipitation of wide coverage and homogeneously distributed stratiform clouds, this time and space lag between the aircraft and the lidar measurements has minor effects on the comparison. This is also confirmed by the very limited variability of the radar reflectivity profiles at 1.29 and 35.5 GHz in the 90-min period (1430–1600 UTC) following the end of the lidar measurements [not shown here but illustrated in Figs. 3 and 4 of Di Girolamo et al. (2012a)]; this very limited variability indicates a lack of local-scale meteorological variability during this period.
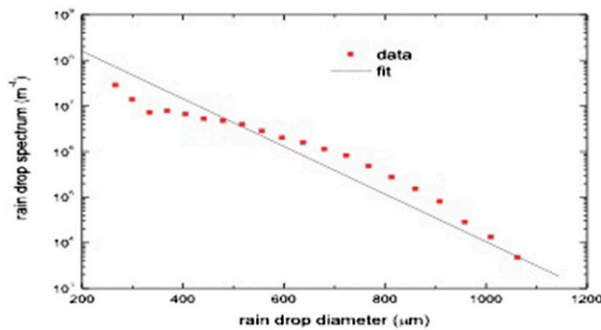
FIG. 5. Particle size spectrum at 2 km as obtained from the rain radar operating at 24.15 GHz and located in the proximity of the Raman lidar system BASIL during the COPS experiment.
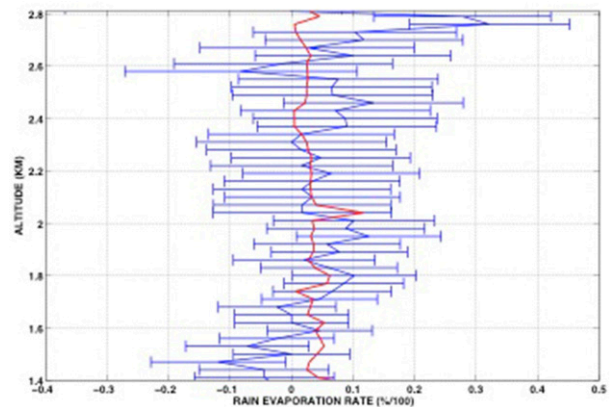

FIG. 6. Raindrop evaporation rate (%/100, blue line) and comparison with the model analytical solution (red line). In the first 200 m below the cloud base, the melting process is not completely ended and the rain is mixed with few snowflakes. This determines a strong evaporation (volume shrinkage > 20%) that is partially fictitious and unrealistic. Breakdown is not taken into account by the model. This can explain the differences in the lidar data in the 1.4–1.8-km atmospheric layer. Negative values represent a volume growth of the raindrop.

Values of D_0 for this case study obtained with our approach based on the application of Eq. (5) are also found to be in good agreement with those obtained from the simultaneous and collocated particle size distribution measurements at 2 km AGL carried out by the rain radar operating at 24.15 GHz (Di Girolamo et al. 2012a; also illustrated here in Fig. 5). At 2 km the precipitating particles are primarily raindrops. These size distribution measurements have been least squares fitted with the Marshall–Palmer size distribution function, obtaining a mean diameter D_0 of $190 \pm 2\,\mu m$, which is in very good agreement with the value of $189 \pm 25\,\mu m$ obtained with our approach. The size range reported above based on the application of Eq. (4) is also in agreement with the results from other rain events, as found in Lolli et al. (2013a). The model analytical solution for D_0 (also reported in Fig. 3a, red line) is calculated assuming constant values for the water vapor mixing ratio and temperature within each layer; these values are taken from the simultaneous and collocated radiosonde profile (launched from the lidar station at 1406 UTC 23 July 2007). In this respect, it is to be noticed that even when launched from the same location as the lidar, the radiosonde is not perfectly collocated with the vertical column illuminated by the lidar, as in fact the former may have drifted horizontally with the wind during its ascent. However, the radiosonde data considered in this case study indicate an overall horizontal drift not exceeding 1.8 km at 3 km—altitude that [together with the very limited variability of the radar reflectivity profiles at 1.29 and 35.5 GHz, again not shown here but illustrated in Figs. 3 and 4 of Di Girolamo et al. (2012a)] testifies that the air masses sounded by the lidar and the radiosonde are substantially the same.

Figure 3a reveals a small difference between the analytical model and the lidar in the altitude region between 1.65 and 1.8 km. In this respect, we can speculate that in this atmospheric region, the model assumptions are no longer valid and that the atmosphere is not in a steady condition. Figure 6 compares the vertical profile of the evaporation rate, defined as in Eq. (1), obtained from lidar measurements (blue), and that from the analytical model solution (red). Lidar data show that evaporation occurs primarily in the first 400–500 m below the cloud base (down to 2.8 km), with a median volume raindrop diameter reduction in excess of 20%, possibly associated with mixed phase/melting, while in the remaining portion of precipitation down to 1.4-km diameter the reduction is smaller. It is to be noticed that the lidar measurements catch a much larger variability in the evaporation process than the model. Large negative values in the lidar-based estimate of evaporation rate profile are found between 2.6 and 2.8 km. We can speculate that these large negative values are partially unrealistic and attributable to the progression of the melting process, partially masking evaporation. This speculation is confirmed by the aircraft in situ measurements, which reveal that melting is still progressing in the first 400–500 m below the cloud base. To obtain a proper quantitative assessment of the agreement between the model and the measurements, the root-mean-square (RMS) deviation, the bias, and the correlation coefficient (CC; Lolli et al. 2014b, 2013b) of model versus lidar data for D_0 have been computed and were 40.23 μm (22%), $-6.05\,\mu m$ (-4%), and 0.65, respectively. Small values for the RMS deviation and the bias and the large value for the correlation coefficient testify the good agreement between the model and lidar results.
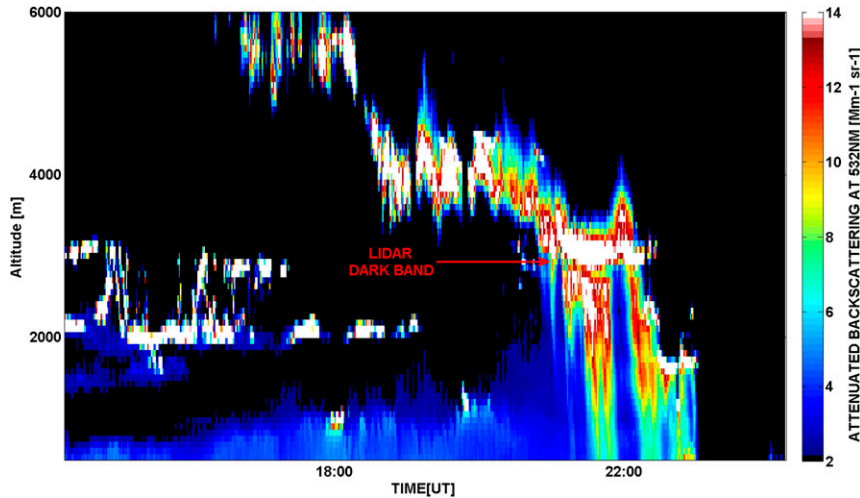
FIG. 7. Attenuated backscattering coefficient composite plot on 9 May 2012 as measured by the MPL system at the GSFC MPLNET permanent observational site.

The second case study reported in this paper refers to a rainfall episode having similar characteristics to the previous one, that is, a stratiform precipitation event originating from the melting layer and not reaching the ground as a result of particle evaporation/sublimation (see Fig. 7). Data were collected on 9 May 2012 (at 2143 UTC; lidar data to retrieve raindrop diameter have a spatial resolution of 75 m and a temporal resolution of 1 min) at NASA GSFC, a permanent observational site of the MPLNET lidar network (Lolli et al. 2013a). Again, a lidar dark band is clearly visible at around 2.9 km, denoting a change in phase from solid to liquid of the hydrometeors. The intercomparison of the lidar and the analytical model in terms of the median volume raindrop diameter and rain evaporation rate are illustrated in Figs. 8 and 9, respectively. Figure 8 reveals that the model profile properly reproduces the lidar profile, except for the sharp increase in size of the median volume diameter at around 1.8 km, which is caught by the lidar data but is not present in the model profile. Again, a quantitative assessment of the agreement between the analytical model and the measurements is given by the RMS deviation, the bias, and the correlation coefficient, having values of 106.62 μm (56%), -9 μm (8%), and 0.56 respectively. Figure 9 shows higher oscillations—both negative and positive—of the change in percentage of raindrop volume diameter during precipitation. With respect to the other analyzed case, the changes of the evaporation rate are bigger. For this case, the larger discrepancies with respect to the first selected case may be imputed to the different air mass sounded by the WMO radiosonde, launched at 0000 UTC (75 min later with respect to the analyzed precipitation) of 10 May 2012 at Washington

Dulles International Airport, 50 km away from the Goddard Space Flight Center. Nevertheless, the agreement between the lidar and the analytical model is still very good, between 0.9 and 1.4 km.

4. Conclusions

A comparison between the model analytical solution proposed by Li and Srivastava (2001) and estimates obtained from multiwavelength lidar data in terms of the median volume raindrop diameter and rain evaporation rate was carried out for two selected case studies: one collected on 23 July 2007 by the Raman lidar system BASIL during the COPS experiment and one collected on 9 May 2012 by the Micropulse Lidar deployed at the NASA GSFC permanent MPLNET observational site. The first experiment was carried out with a single research multiwavelength lidar (BASIL), while the second one was carried out with two separate and collocated
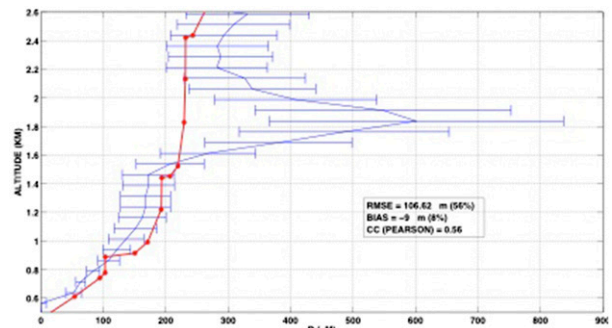

FIG. 8. Vertical profile of the median volume raindrop diameter D_0 (together with its error bar) as determined from the lidar measurements at 2143 UTC 9 May 2012. The red line represents the model analytical solution calculated as described in section 2b.
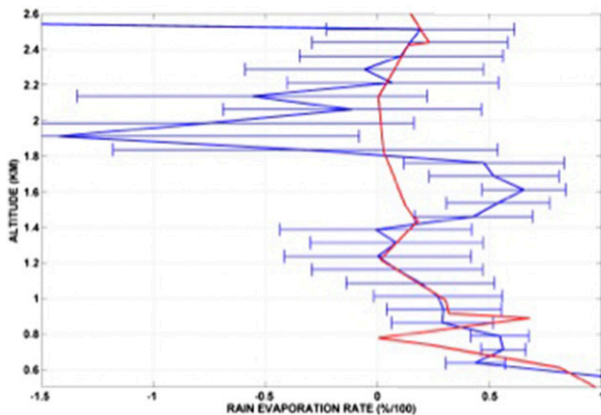
FIG. 9. Raindrop evaporation rate (%/100) and comparison with the model analytical solution (red line).

commercial lidars (Leosphere and Micropulse) at two different wavelengths.

These two comparisons reveal that, accounting for the measurement error, the analytical model solution is in good agreement with the measurements in large portions of the sampled precipitation interval. Some local discrepancies may be the result of (i) the melting process being not completed yet and, consequently, leading to false retrievals when assuming particles to be spherical; (ii) the statistical uncertainty affecting lidar measurements being large enough to determine spurious structures in the retrieved profiles of both the median volume raindrop diameter and rain evaporation rate; and (iii) some of the hypotheses considered in the model being no longer valid, especially for vertical drop coalescence and drop break-down (1.4–1.8 km in the first case). An additional source of potential deviations may be associated with the nonperfect collocation of the radiosonde ascent path and the vertical column above the lidar station, as in fact the radiosonde drifted horizontally during its ascent, and consequently different air masses may be sounded by the lidar and the radiosonde. This is especially true for the second selected case, were the radiosonde was launched 2 h later at a distance of 50 km from lidar observational site. Furthermore, in the determination of the median volume raindrop diameter and the evaporation rate, it is to be pointed out that the consideration of an integration time for both virga and nonvirga lidar profiles has no implication on the illustrated results. In fact, the environmental cooling associated with the evaporation or sublimation of the melting particles during the virga event has marginal effects on the raindrop diameter or the evaporation rate results in the altitude region of interest for this study (above 1 km), which is a region where thermal effects on the melting environment associated with the hydrometeors' absorption of latent heat are limited.

The comparisons illustrated in this paper allowed for testing of the limits of the proposed method, which shows larger errors when raindrop diameters are larger than 500 μm as the color ratio curves become flatter (Fig. 1c). However, in the future we intend to possibly extend the application of the technique described and tested in the present paper to the MPLNET database and, based on the combination of single-wavelength lidar measurements with in situ disdrometer data (at those stations where these are available) and the above-illustrated analytical model, build up a climatology of the raindrop diameter and evaporation rate profiles from the ground up to the cloud base over an extended area and period of time.

REFERENCES

Bedard, A. J., Jr., 2003: Aviation weather hazards. *Encyclopedia of Atmospheric Science*, J. R. Holton, J. A. Pyle, and J. A. Curry, Eds., Vol. 1, Academic Press, 166–177.

Blanchard, D. C., 1953: Raindrop size-distribution in Hawaiian rains. *J. Meteor.*, **10**, 457–473, doi:10.1175/1520-0469(1953)010<0457:RSDIHR>2.0.CO;2.

Bringi, V. N., and V. Chandrasekar, 2001: *Polarimetric Doppler Weather Radar: Principles and Applications*. Cambridge University Press, 636 pp.

Campbell, J. R., D. Hlavka, E. Welton, C. Flynn, D. Turner, J. Spinhirne, V. Scott, and I. Hwang, 2002: Full-time, eye-safe cloud and aerosol lidar observation at Atmospheric Radiation Measurement program sites: Instrument and data processing. *J. Atmos. Oceanic Technol.*, **19**, 431–442, doi:10.1175/1520-0426(2002)019<0431:FTESCA>2.0.CO;2.

Demoz, B., D. Starr, D. Whiteman, K. Evans, D. Hlavka, and R. Peravali, 2000: Raman LIDAR detection of cloud base. *Geophys. Res. Lett.*, **27**, 1899–1902, doi:10.1029/1999GL010941.

Di Girolamo, P., R. V. Gagliardi, G. Pappalardo, N. Spinelli, R. Velotta, and V. Berardi, 1995: Two wavelength lidar analysis of stratospheric aerosol size distribution. *J. Aerosp. Sci.*, **26**, 989–1001, doi:10.1016/0021-8502(95)00025-8.

——, D. Summa, and R. Ferretti, 2009a: Multiparameter Raman lidar measurements for the characterization of a dry stratospheric intrusion event. *J. Atmos. Oceanic Technol.*, **26**, 1742–1762, doi:10.1175/2009JTECHA1253.1.

——, ——, R.-F. Lin, T. Maestri, R. Rizzi, and G. Masiello, 2009b: UV Raman lidar measurements of relative humidity for the

characterization of cirrus cloud microphysical properties. *Atmos. Chem. Phys.*, **9**, 8799–8811, doi:10.5194/acp-9-8799-2009.

——, ——, M. Cacciani, E. G. Norton, G. Peters, and Y. Dufournet, 2012a: Lidar and radar measurements of the melting layer: Observations of dark and bright band phenomena. *Atmos. Chem. Phys.*, **12**, 4143–4157, doi:10.5194/acp-12-4143-2012.

——, ——, R. Bhawar, T. Di Iorio, M. Cacciani, I. Veselovskii, O. Dubovik, and A. Kolgotin, 2012b: Raman lidar observations of a Saharan dust outbreak event: Characterization of the dust optical properties and determination of particle size and microphysical parameters. *Atmos. Environ.*, **50**, 66–78, doi:10.1016/j.atmosenv.2011.12.061.

Gori, E. G., and J. Joss, 1980: Changes of shape of raindrop size distributions simultaneously observed along a mountain slope. *J. Rech. Atmos.*, **14**, 239–300.

Kalthoff, N., and Coauthors, 2011: The dependence of convection-related parameters on surface and boundary-layer conditions over complex terrain. *Quart. J. Roy. Meteor. Soc.*, **137**, 70–80, doi:10.1002/qj.686.

Leary, C. A., and R. A. Houze Jr., 1979: Melting and evaporation of hydrometeors in precipitation from the anvil clouds of deep tropical convection. *J. Atmos. Sci.*, **36**, 669–679, doi:10.1175/1520-0469(1979)036<0669:MAEOHI>2.0.CO;2.

Levin, Z., G. Feingold, S. Tzivion, and A. Waldvogel, 1991: The evolution of raindrop spectra: Comparisons between modeled and observed spectra along a mountain slope in Switzerland. *J. Appl. Meteor.*, **30**, 893–900, doi:10.1175/1520-0450(1991)030<0893:TEORSC>2.0.CO;2.

Li, X., and R. Srivastava, 2001: An analytical solution for raindrop evaporation and its application to radar rainfall measurements. *J. Appl. Meteor.*, **40**, 1607–1616, doi:10.1175/1520-0450(2001)040<1607:AASFRE>2.0.CO;2.

——, W.-K. Tao, A. P. Khain, J. Simpson, and D. E. Johnson, 2009: Sensitivity of a cloud-resolving model to bulk and explicit bin microphysical schemes. Part II: Cloud microphysics and storm dynamics interactions. *J. Atmos. Sci.*, **66**, 22–40, doi:10.1175/2008JAS2647.1.

Lolli, S., L. Sauvage, S. Loaec, and M. Lardier, 2011: EZ Lidar™: A new compact autonomous eye-safe scanning aerosol Lidar for extinction measurements and PBL height detection. Validation of the performances against other instruments and intercomparison campaigns. *Opt. Pura Apl.*, **44** (1), 33–41.

——, E. J. Welton, and J. R. Campbell, 2013a: Evaluating light rain drop size estimates from multiwavelength Micropulse Lidar Network profiling. *J. Atmos. Oceanic Technol.*, **30**, 2798–2807, doi:10.1175/JTECH-D-13-00062.1.

——, A. Delaval, C. Loth, A. Garnier, and P. H. Flamant, 2013b: 0.355-micrometer direct detection wind lidar under testing during a field campaign in consideration of ESA's ADM-Aeolus mission. *Atmos. Meas. Tech.*, **6**, 3349–3358, doi:10.5194/amt-6-3349-2013.

——, E. J. Welton, J. R. Campbell, E. Eloranta, B. N. Holben, B. N. Chew, and S. V. Salinas, 2014a: High Spectral Resolution Lidar and MPLNET Micro Pulse Lidar aerosol optical property retrieval intercomparison during the 2012 7-SEAS field campaign at Singapore. *Lidar Technologies, Techniques, and Measurements for Atmospheric Remote Sensing, X*, U. N.

Singh and G. Pappalardo, Eds., International Society for Optical Engineering (SPIE Proceedings, Vol. 9246), 92460C, doi:10.1117/12.2067812.

——, ——, A. Benedetti, L. Jones, M. Suttie, and S.-H. Wang, 2014b: MPLNET lidar data assimilation in the ECMWF MACC-II Aerosol system: Evaluation of model performances at NCU lidar station. *Lidar Technologies, Techniques, and Measurements for Atmospheric Remote Sensing, X*, U. N. Singh and G. Pappalardo, Eds., International Society for Optical Engineering (SPIE Proceedings, Vol. 9246), 92460I, doi:10.1117/12.2068201.

——, J. Lewis, J. R. Campbell, Y. Gu, and E. Welton, 2016: Cirrus cloud radiative characteristics from continuous MPLNET profiling at GSFC in 2012. *Opt. Pura Apl.*, **49**, 1–6, doi:10.7149/OPA.49.1.1.

Marshall, J. S., and W. Mc K. Palmer, 1948: The distribution of raindrops with size. *J. Atmos. Sci.*, **5**, 165–166, doi:10.1175/1520-0469(1948)005<0165:TDORWS>2.0.CO;2.

Morrison, H. G., G. Thompson, and V. Tatarskii, 2009: Impact of cloud microphysics on the development of trailing stratiform precipitation in a simulated squall line: Comparison of one- and two-moment schemes. *Mon. Wea. Rev.*, **137**, 991–1007, doi:10.1175/2008MWR2556.1.

O'Connor, E. J., R. J. Hogan, and A. J. Illingworth, 2005: Retrieving stratocumulus drizzle parameters using Doppler radar and lidar. *J. Appl. Meteor.*, **44**, 14–27, doi:10.1175/JAM-2181.1.

Spinhirne, J. D., 1993: Micro pulse lidar. *IEEE Trans. Geosci. Remote Sens.*, **31**, 48–55, doi:10.1109/36.210443.

——, J. A. R. Rall, and V. S. Scott, 1995: Compact eye-safe lidar system. *Rev. Laser Eng.*, **23**, 112–118, doi:10.2184/lsj.23.112.

Tan, F., and Coauthors, 2014: Variation in daytime tropospheric aerosol via LIDAR and sunphotometer measurements in Penang, Malaysia. *AIP Conf. Proc.*, **1588**, 286, doi:10.1063/1.4866962.

Ulbrich, C. W., and D. Atlas, 1998: Rainfall microphysics and radar properties: Analysis methods for drop size spectra. *J. Appl. Meteor.*, **37**, 912–923, doi:10.1175/1520-0450(1998)037<0912:RMARPA>2.0.CO;2.

Welton, E. J., and Coauthors, 2002: Measurements of aerosol vertical profiles and optical properties during INDOEX 1999 using micropulse lidars. *J. Geophys. Res.*, **107**, 8019, doi:10.1029/2000JD000038.

Westbrook, C. D., R. J. Hogan, E. J. O'Connor, and A. J. Illingworth, 2010: Estimating drizzle drop size and precipitation rate using two-colour lidar measurements. *Atmos. Meas. Tech.*, **3**, 671–681, doi:10.5194/amt-3-671-2010.

Worden, J., and Coauthors, 2007: Importance of rain evaporation and continental convection in the tropical water cycle. *Nature*, **445**, 528–532, doi:10.1038/nature05508.

Wulfmeyer, V., and Coauthors, 2011: The Convective and Orographically-induced Precipitation Study (COPS): The scientific strategy, the field phase, and research highlights. *Quart. J. Roy. Meteor. Soc.*, **137**, 3–30, doi:10.1002/qj.752.

Xie, X., R. Evaristo, S. Troemel, P. Saavedra, C. Simmer, and A. Ryzhkov, 2016: Radar observation of evaporation and implications for quantitative precipitation and cooling rate estimation. *J. Atmos. Oceanic Technol.*, **33**, 1779–1792, doi:10.1175/JTECH-D-15-0244.1.